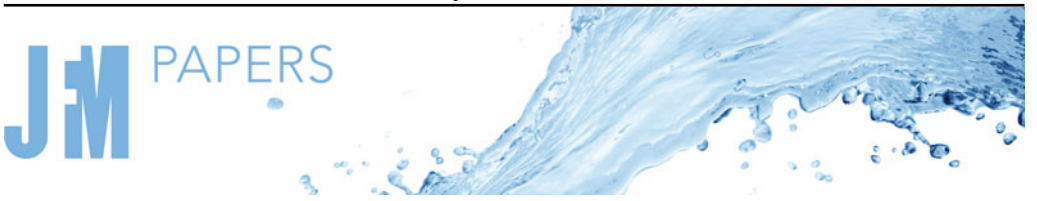
J. Fluid Mech. (2026), *vol.* 1041, A4, doi:10.1017/jfm.2026.11904



Third-order first-harmonic radiation by a semi-immersed sphere in forced heave motion

Bryan Tan[1], **Hugh A. Wolgamot**[1,2], **Jana Orszaghova**[1,2,3], **Adi Kurniawan**[1,2] **and Jørgen Hals Todalshaug**[4]

[1]School of Earth and Oceans, University of Western Australia, Crawley, WA, Australia

[2]Marine Energy Research Australia, University of Western Australia, Albany, WA, Australia

[3]Blue Economy Cooperative Research Centre, Launceston, TAS, Australia

[4]CorPower Ocean, Stockholm, Sweden

Corresponding author: Bryan Tan, bryan.tan@research.uwa.edu.au

(Received 2 April 2026 UTC; revised 12 June 2026 UTC; accepted 30 June 2026 UTC)

Nonlinear hydrodynamic effects influence the power capture of resonant wave energy converters (WECs), particularly within the frequency band where these devices are designed to operate. In this study, wave flume experiments are conducted on a semi-immersed spherical model with prescribed heave motions, emulating the response to an incident broad-banded wave group. Several body motion amplitudes (up to a maximum displacement of greater than half the radius) are tested at different peak frequencies, revealing progressive reductions in both the first-harmonic radiation forces and radiated wave elevations, per unit motion amplitude, as the motion amplitude is increased. A simple partially nonlinear potential flow model incorporating instantaneous 'volume flow' corrections shows very good agreement with the measured radiated waves, capturing the dominant nonlinear trends. An experimental decomposition of the radiated field into channel modes is also performed, based on linear theory while accounting for linear viscous dissipation. This is then used to calculate the power in the radiated field compared to the input power from the moving body over a frequency band of interest. The model and experiments show a consistent, monotonic decrease in normalised radiated power as the amplitude of body motion increases. Overall, the findings indicate that linear theory is remarkably accurate even for quite large body motions. The most important nonlinear corrections in the first-harmonic frequency range arise from third-order potential flow interactions, fundamentally caused by the spherical geometry, and demonstrate the potential utility of volume flow models for assessing WEC radiation.

Key words: surface gravity waves, wave-structure interactions

© The Author(s), 2026. Published by Cambridge University Press. This is an Open Access article, distributed under the terms of the Creative Commons Attribution licence (https://creativecommons.org/licenses/by/4.0/), which permits unrestricted re-use, distribution and reproduction, provided the original article is properly cited.

https://doi.org/10.1017/jfm.2026.11904 Published online by Cambridge University Press

1. Introduction

The hydrodynamic interaction between surface gravity waves and floating structures is often analysed for naval, oil and gas, and offshore renewable energy applications. The motion of these structures in the ocean creates radiated waves due to the displacement of the fluid, which affects the pressure field around the structure. The integration of this pressure over the body's wetted surface is known as the radiation force. If the body motions are relatively small, then the equilibrium wetted surface can be considered and the radiated field calculated using linear potential flow theory (omitting viscous effects). If, however, the wetted surface changes substantially due to large motions of the body (e.g. at resonance), then more complicated nonlinear models are required to accurately predict the behaviour. Within a potential flow theory framework, nonlinearity arises due to the nonlinear free-surface boundary condition and/or the body boundary condition on the instantaneous immersed hull. Weakly nonlinear models utilise a perturbation expansion, and formulate and solve the problem at different orders, while fully nonlinear models retain the exact nonlinear boundary conditions. Since fully nonlinear models are too computationally intensive for real-time control or rapid design iterations, there is substantial interest in efficient nonlinear representations to support the development and optimisation of wave energy converters (WECs) (Penalba *et al.* 2017; Davidson & Costello 2020).

The radiation problem has been studied extensively. For example, Gu *et al.* (2018) investigated the radiation force on common WEC float geometries in forced oscillations and the importance of viscous effects in each geometry; Drake *et al.* (2009) instead used a heaving cone to exemplify the limitations of first- and second-order theory when considering 'flared' geometries above the waterline; and Kramer *et al.* (2021) conducted highly controlled free-decay tests of a sphere from various initial displacements as benchmark data to compare against several independently formulated numerical models. Kashiwagi (1989) also conducted radiation tests with a spherical model in a wave flume (with very similar dimensions to the current study), showing very good agreement with linear theory. However, the motion amplitudes were not stated, making it difficult to infer the nonlinear behaviour. Third-order radiation effects were explicitly studied by Vantorre (1986*a*,*b*, 1990), especially the importance of the first-harmonic component for WECs, and theoretical third-order corrections of the added mass and radiation damping for axisymmetric bodies were presented. However, the accompanying experimental results were greatly limited by several factors: only three amplitudes were tested, the input motions were monochromatic, and the tests were conducted in a fairly small testing tank ($4 \times 4 \times 1$ m^3), which inevitably contaminated results with reflections. To the authors' knowledge, there are no other existing studies that explicitly identify and model third-order first-harmonic radiation terms (which scale cubically with the input amplitude but share a similar frequency range with the linear response). Forced oscillations of structures with heave plates have exhibited significant amplitude dependence in the heave added mass and damping coefficients derived from the first-harmonic force (Han *et al.* 2024), but the origins of most of these differences are in the details of the separated flow. Such effects are of great importance for many structures, but are not our focus, and are typically avoided (where possible) in WECs. Similarly, Orszaghova *et al.* (2021) investigated nonlinear odd-harmonic resonant motions of an offshore wind floater at frequencies below the lower limit of the linear wave spectrum, and concluded that these were caused by viscous drag effects rather than third-order first-harmonic potential flow forcing. These nonlinear terms possess wider bandwidths due to the 'spectral smearing' discussed in § 7, and thus excite frequencies below and above the linear frequency range. Fully nonlinear potential flow

https://doi.org/10.1017/jfm.2026.11904 Published online by Cambridge University Press

numerical studies (e.g. Dommermuth & Yue 1987; Bai & Eatock Taylor 2006) have also been conducted, and while these studies inherently include all nonlinearities, they have not analysed the amplitude dependence of the first-harmonic force specifically. Body-exact models with linear free-surface boundary conditions but nonlinear body boundary conditions have been derived (Ferrant 1991) and used to study radiation by a heaving semi-immersed sphere (Lin & Yue 1991). Most other studies of third-order interactions instead consider the third-harmonic component for its application to high-frequency resonances of fixed structures (Faltinsen *et al.* 1995; Malenica & Molin 1995; Teng & Kato 2002). We therefore make various references to Tan *et al.* (2025), a related study that identified and modelled third-order first-harmonic exciting forces on a sphere (as opposed to the radiation terms explored here) using a combination of phase-based harmonic separation techniques and amplitude scaling properties. Some of the same analysis methodologies are adopted here, but the results, modelling and discussion are new.

In this work, we first present a review of potential flow theory and the corresponding nonlinear terms from a perturbation expansion. This is followed by an overview of the experimental set-up and instrumentation of wave flume experiments where a half-immersed spherical model, representing a typical point absorber WEC, was actuated in heave to investigate the resultant radiated waves and radiation force. Experimental results are then presented, focusing specifically on the first-harmonic nonlinearities, as they coincide with the operational frequency range of WECs and therefore directly influence their performance. To assist with subsequent intepretation of results, a brief discussion of the linear radiation problem for a body in a channel is presented. A partially nonlinear potential flow numerical model with instantaneous 'volume flow' corrections is then developed to capture the dominant nonlinear effects in the radiated field. Experimental results are then digested into a form allowing comparison with standard frequency-domain coefficients from linear theory, and the volume flow model, as appropriate. To further interrogate the results, we show the amplitude dependence of the radiated power in the near and far fields over a truncated frequency range, accounting for the influence of viscous effects.

2. The weakly nonlinear wave radiation problem

Wave–structure interactions are often simplified using linear potential flow theory where the input, in this case the forced displacement of the body ζ, is proportional to the output, the radiation force F and the radiated waves η generated. This formulation is ubiquitous and formally derived in most hydrodynamics textbooks such as Newman (2017) and Falnes & Kurniawan (2020). For a spherical body undergoing large oscillatory heave motions, representative of an operating point absorber WEC, a limitation is that effects such as the instantaneous change in submerged volume, $V(t) - V_0$, are linearised such that $V(t) - V_0 \approx -S_0\,\zeta(t)$, using the mean waterplane area S_0. This prismatic approximation of the change in submerged volume is formally valid only for infinitesimal motion amplitudes, but in practice performs very well over a relatively large range. There is great interest in determining how well linear theory performs, and how large the most important corrections are in the wave frequency range.

Since this study focuses entirely on first-harmonic nonlinearities that are most relevant for power capture, we consider mild to moderate motion amplitudes where the wave–structure interaction remains weakly nonlinear. For such a system, any output such as the radiation force or radiated waves can be represented by a Stokes perturbation expansion

$$F(t) = F^{(11)}(t) + F^{(20)}(t) + F^{(22)}(t) + F^{(31)}(t) + F^{(33)}(t) + \mathcal{O}(A^4), \qquad (2.1)$$

https://doi.org/10.1017/jfm.2026.11904 Published online by Cambridge University Press

where the superscript (pq) indicates a term of pth order and qth harmonic, i.e. a term that scales with the input amplitude A to the pth power, and appears around q times the peak frequency f_p in the frequency domain. Therefore, $F^{(11)}$ is simply the first-order first harmonic (linear term), and $F^{(31)}$ is the third-order first harmonic, a term that scales cubically with the amplitude but shares a similar frequency range with the linear term.

In this work, we use a broad-banded motion input with phases of all Fourier components deterministically aligned. Such a focused motion signal (analogous to a focused wave; see Tromans *et al.* 1991; Taylor & Williams 2004) is given by

$$\zeta_\psi(t) = \sum_i \mathcal{A}_i \cos(\omega_i t + \psi), \tag{2.2}$$

where $\mathcal{A}_i$ is the Fourier amplitude corresponding to a component with angular frequency ω_i, and ψ is the focus phase prescribed to all frequency components. The envelope peak of the displacement input is then $A = \sum_i \mathcal{A}_i$. If we use two motion inputs π phase apart to generate corresponding radiation forces F_ψ and $F_{\psi+\pi}$, and combine them in the form

$$F_{odd}(t) = \frac{1}{2}\left(F_\psi(t) - F_{\psi+\pi}(t)\right) = F^{(11)}(t) + F^{(31)}(t) + F^{(33)}(t) + \mathcal{O}(A^5), \tag{2.3}$$

then we can isolate the odd harmonics of the output radiation force (or alternatively the output radiated waves). Since the even harmonics $F^{(20)}$ and $F^{(22)}$ often overlap with the first-harmonic frequency range and contaminate the results, this method allows cleaner isolation of the first harmonic. Applying a simple low-pass filter in (2.3) is then sufficient to isolate the first-harmonic terms $F^{(11)} + F^{(31)}$ from the higher harmonics. Phase-based harmonic separation methods have been applied in many hydrodynamic studies (e.g. Fitzgerald *et al.* 2014; Zhao *et al.* 2017; Chen *et al.* 2018; Vyzikas *et al.* 2018; Hlophe *et al.* 2025; Liu *et al.* 2025). Further decomposition into $F^{(11)}$ and $F^{(31)}$ is, however, non-trivial for experimental data (Tan *et al.* 2025), therefore the total first harmonic $F^{(1)} = F^{(11)} + F^{(31)} + \mathcal{O}(A^5)$ is analysed in the remainder of this paper.

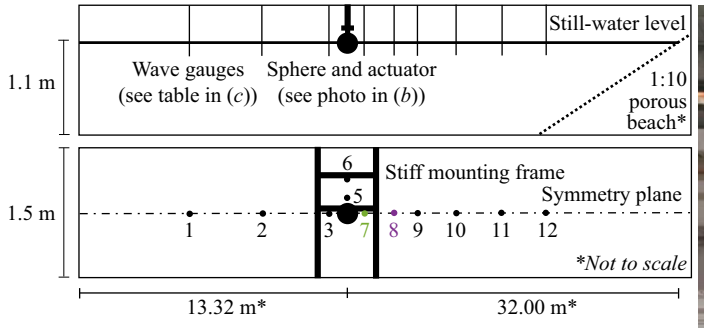
3. Experimental method

The experiments were conducted at the Coastal and Offshore Research Laboratory, University of Western Australia. A schematic of the layout and key dimensions can be seen in figure 1(*a*). The set-up comprised a LinMot actuator (model no. P01-48x240F-SSC) to impose the heaving motion of the sphere, an Interface 3-axis 50 N load cell (model no. 3A120) to measure the force on the sphere, and an array of Edinburgh Designs wave gauges (model no. WG8USB) to measure the radiated waves (gauge locations detailed in figure 1(*c*)). While the imposed motion of the sphere was recorded by the actuator, we also implemented several external displacement measurement instruments: a Penny & Giles linear displacement transducer (model no. SLS130), a LinMot magnetic strip linear encoder (model no. MS01-1/D-SSI) and a Qualisys motion capture system (model no. 5+) to ensure that the input motions were known accurately – all displacement measurements were found to be consistent to within 0.1 %. An annotated photo of these instruments is shown in figure 1(*b*). Most instruments were sampled at 128 Hz or higher, and all of them were synchronised through an electronic trigger. The aluminium sphere model had radius $R = 0.126 \pm 0.001$ m. The water depth was 1.1 m.

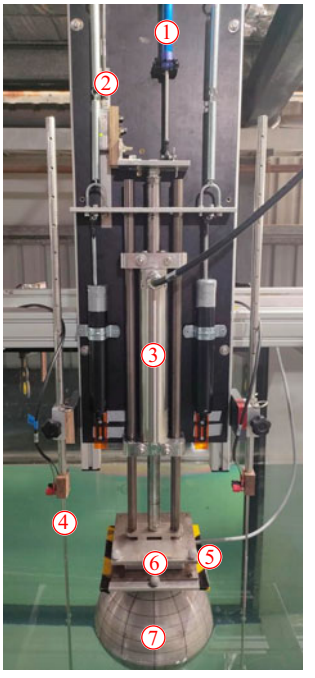
The demand motion signals were compact NewWave-type signals (Tromans *et al.* 1991; Taylor & Williams 2004) with underlying spectra of JONSWAP type (with peak enhancement factor $\gamma = 2.5$) defined across frequencies from 0 to $2.5 f_p$. Three peak

https://doi.org/10.1017/jfm.2026.11904 Published online by Cambridge University Press

(a)



(b)



(c)

Wave gauge no.	x (m)	y (m)
1	–8.13	0
2	–4.12	0
3	–0.20	0
4	0	0
5	0	0.19
6	0	0.39
7	**0.22**	**0**
8	**3.92**	**0**
9	7.92	0
10	11.72	0
11	16.72	0
12	21.72	0

Figure 1. (*a*) Schematic of the experimental set-up. (*b*) Corresponding photo with annotated instrumentation: ① linear displacement transducer, ② magnetic strip linear encoder, ③ linear actuator, ④ wave gauge 3, ⑤ Qualisys marker, ⑥ load cell, ⑦ model sphere. (*c*) The wave gauge locations are relative to the sphere centre, and the coloured numbers indicate the gauges referenced in figure 5. Note that wave gauge 4 is not used in these radiation tests.

frequencies $f_p = 0.4, 0.6, 0.8$ Hz, six amplitudes $A = 0.02, 0.03, 0.04, 0.05, 0.06, 0.07$ m (corresponding to the envelope peak of the motion signal), and two focus phases $[\psi, \psi + \pi] = [3\pi/2, \pi/2]$ (up- and down-crossing focused displacement signals) were tested. However, for brevity, only plots of the experimental data for $f_p = 0.8$ Hz are presented in the following sections, and the data from the other two peak frequencies are presented in Appendix A.

We note that while it would have been ideal to position the sphere equidistantly from both ends of the flume to maximise the available time prior to reflections, these tests are part of a larger campaign that included tests with incident waves, so a compromise was made to position the sphere further from the beach (and thus closer to the wavemaker, which was not used in these tests). This short distance to the wavemaker inevitably affected the way measurements were analysed, as further discussed in § 7.

Here, we discuss the extraction of the radiation force from the total force measured by the load cell. By nature of the testing set-up, the total force on the load cell F_{LC} is dominated by the inertial F_{IN}, the hydrostatic F_{HS} and weight F_G forces on the sphere, whereas the desired hydrodynamic radiation force makes up only ~ 15 % of the measured force at most, and much less in many cases. The isolated radiation force on the sphere is thus given by

$$F(t) = F_{LC}(t) - F_{HS}(t) - F_{IN}(t) - F_G. \tag{3.1}$$

https://doi.org/10.1017/jfm.2026.11904 Published online by Cambridge University Press

This leads to two main challenges: first, the estimation of the inertial and hydrostatic forces has to be very accurate to ensure that their contributions are properly removed, and second, the small absolute magnitude of the radiation force means that the signal-to-noise quality is much lower than e.g. a diffraction test where the entirety of the measured dynamic force is used (Tan *et al.* 2025). Dry tests of every condition were thus conducted to measure the inertial force on the load cell while the set-up was actuated in air. Theoretically, one could also conduct dedicated tests to directly measure the hydrostatic force by slowly changing the draft of the sphere in still water. Unfortunately, the slow drift of the load cell over the long times necessary for such a test was found to substantially affect these measurements, so the hydrostatic force had to instead be indirectly estimated from $F_{HS}(t) = \rho g V(t)$. The volume beneath the mean free surface was calculated using the body displacements and volume profile, with the latter measured by a HandySCAN three-dimensional laser scanner (model no. BLACK Elite) with accuracy 0.025 mm. The radiated wave measurements, on the other hand, do not require this post-processing, although they are of the order of millimetres and thus are also affected by low signal-to-noise ratio. Repeated tests conducted across three different days were found to have root mean square error 0.1 mm in the wave measurements, and 0.1 N in the force measurements. No wave breaking was observed.

4. Experimental results

The input displacement and the extracted first-harmonic radiation forces and radiated wave time series are plotted in figure 2. All six amplitudes of the $f_p = 0.8$ Hz condition are plotted, with darker lines representing smaller amplitude motions, and progressively lighter colours denoting the larger amplitudes. The black lines (figures 2*a*,*b*) show the imposed heave displacement $\zeta(t)$, the blue lines (figures 2*c*,*d*) show the vector projection of the radiation force onto the displacement $(F^{(11)}(t) + F^{(31)}(t))_{\parallel \zeta(t)}$ ('the added mass portion of the radiation force'), the orange lines (figures 2*e*,*f*) show the corresponding vector rejection $(F^{(11)}(t) + F^{(31)}(t))_{\perp \zeta(t)}$ ('the radiation damping portion'), and the green lines (figures 2*g*,*h*) show the radiated wave elevation from a wave gauge close to the sphere (wave gauge 7 in figure 1). Figures 2(*a*,*c*,*e*,*g*) are the raw signals, while figures 2(*b*,*d*,*f*,*h*) contain the same signals normalised by the displacement envelope peak A (the envelope is partially shown by the dash-dotted line in figure 2*b*).

While the normalised motion time series collapse to high precision (by design), the normalised responses (force and free surface) can be seen to exhibit weakly nonlinear behaviour. The inset plots show that there is an ordered separation of the forces similar to that observed in Tan *et al.* (2025), where it was confirmed to be the result of third-order first-harmonic terms $F^{(31)}$. At the largest displacement amplitude tested ($A/R = 0.56$), the normalised forces appear to be $\sim 10\,\%$ lower than at the smallest amplitude $A/R = 0.16$ – i.e. the first-harmonic radiation force on a sphere undergoing heaving motions of half of its radius can be $10\,\%$ lower than predicted by linear theory. We emphasise again that the exact (to experimental accuracy) hydrostatic contribution relative to still water has been removed here. The level of separation between linear and nonlinear values appears to be comparable between the 'added mass' and 'radiation damping' portions of the radiation force. The radiated waves also clearly show the nonlinear ordering with motion amplitude.

5. The linear radiation problem in a channel

In subsequent sections, results from linear theory are compared to experimental data. It is therefore useful to briefly discuss features of the linear radiation problem that arise as a

https://doi.org/10.1017/jfm.2026.11904 Published online by Cambridge University Press

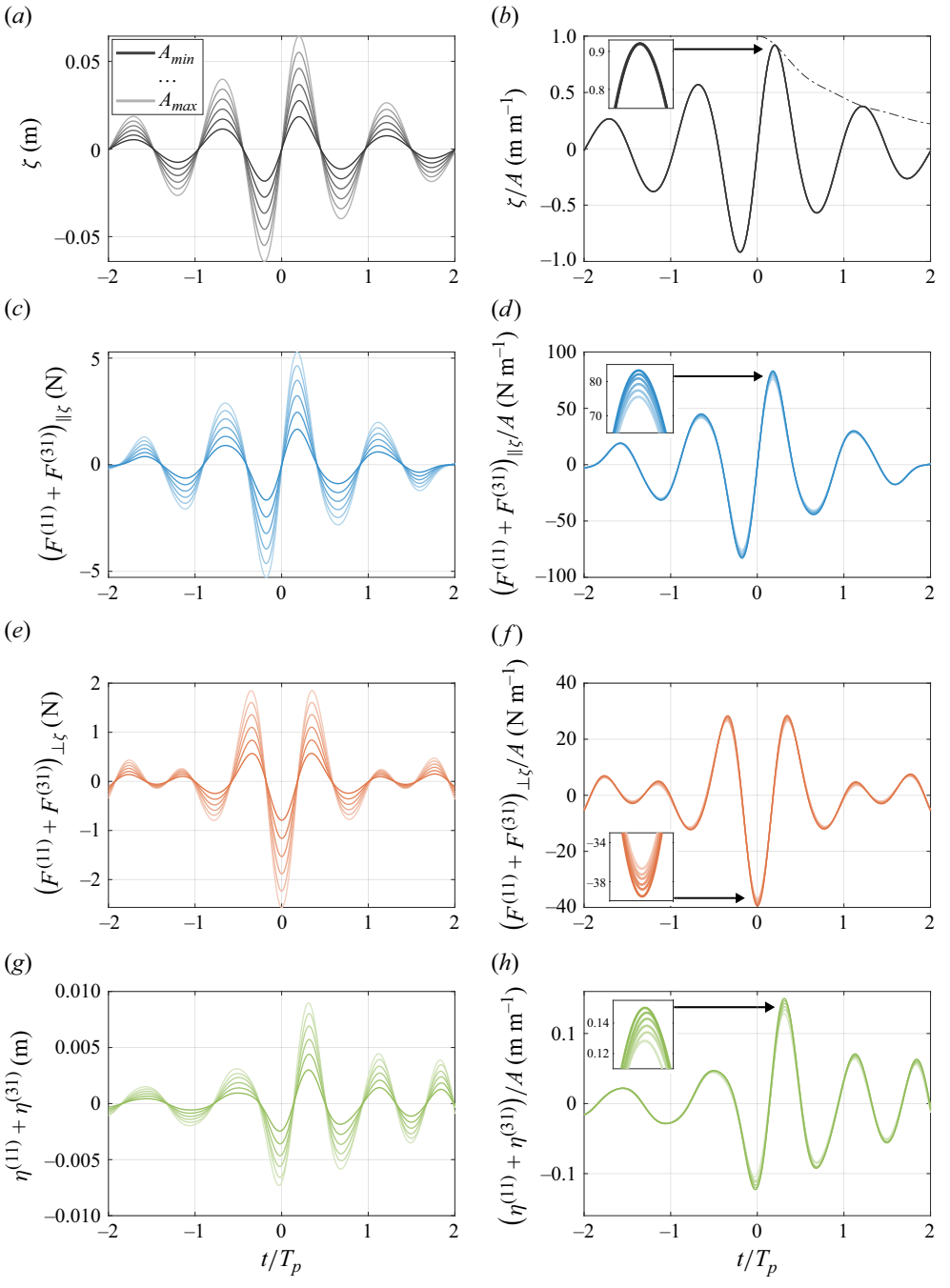


Figure 2. Experimental (*a*,*c*,*e*,*g*) raw and (*b*,*d*,*f*,*h*) normalised first-harmonic (*a*,*b*) body displacement, (*c*,*d*) vector projection and (*e*,*f*) rejection of the radiation force onto the heave displacement (analogous to the added mass and radiation damping coefficients), and (*g*,*h*) radiated free surface. Six input motion amplitudes are shown, where the darker lines represent the smaller input motion amplitudes. The motion envelope is partially shown by the dash-dotted line in (*b*). Peak frequency of the motion input is $f_p = 0.8$ Hz.

https://doi.org/10.1017/jfm.2026.11904 Published online by Cambridge University Press

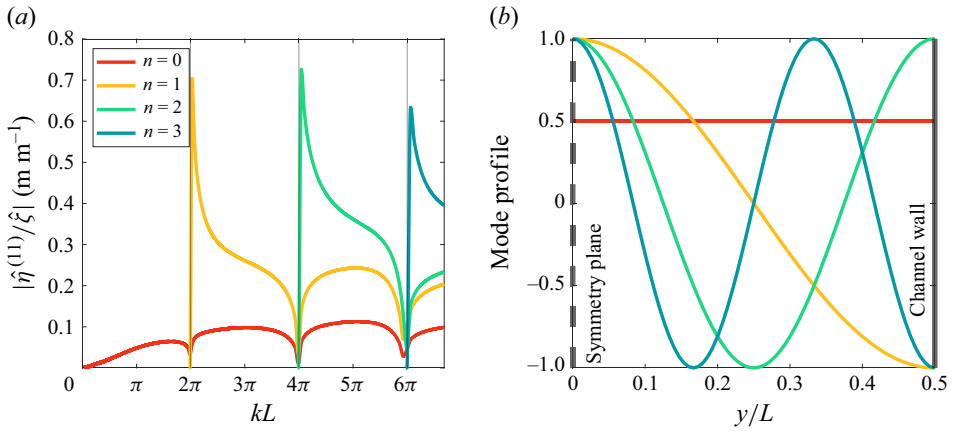


Figure 3. (*a*) Ratio of the linear radiated wave amplitude and displacement amplitude of a sphere in a channel, decomposed into contributions from each channel mode. (*b*) Their respective profiles visualised across the half-width ($L/2$) of the channel. The sphere radius is $R = L/12$.

consequence of testing between parallel walls. For an oscillating body positioned centrally in a channel of total width L, the far-field radiated waves at a finite frequency consist of a discrete set of propagating wave components travelling along ($n = 0$) and at an angle ($n \geq 1$) to the channel, with their profile across the channel proportional to cos ($2n\pi y/L$) and visualised in figure 3(*b*) (note that antisymmetric modes are not excited in linear theory due to the symmetry of the problem). For $n \geq 1$, each mode can be viewed as a pair of obliquely propagating components with propagation angles θ_n and $-\theta_n$.

Solutions to the linear radiation problem for a sphere in a channel were first presented by Kashiwagi (1989). In this work, we use Hydrostar (2016) to solve the heave radiation problem. To elucidate features of the problem, we compute the far-field linear radiated waves emitted by a heaving half-immersed sphere positioned centrally in a channel. The result is shown as a ratio of the radiated wave amplitude to the body displacement in figure 3(*a*) (the radiated waves were calculated at $x = 106R$ from the sphere centre). The thin vertical lines indicate the frequencies where an integer number of wavelengths exactly spans the width of the channel – the cut-off frequencies above which additional channel modes can propagate. Each colour shows the contribution from a given mode, found by decomposing the total into modes present at each frequency. This was calculated utilising the complex amplitudes of the total free-surface elevation from a handful of cross-flume locations, and at each frequency, fitting the relevant mode profiles across the flume width at these locations. The modulus of each fitted modal complex amplitude is what is displayed in figure 3(*a*).

After each successive cut-off frequency, another propagating mode is permitted across the channel, and the total radiated wave measurement at a given location in the flume is therefore subject to the interference of these modes with each other. This causes highly irregular features in the frequency-domain transfer functions at any point in space when $kL > 2\pi$ since contributions from multiple modes are totalled (even though the individual modes follow smooth curves). Some of these irregular features are seen in the linear results in figure 5(*d*) below.

The far-field radiated waves are related to the damping, so the decomposed free-surface amplitudes can also be used in the following equation, adapted from Srokosz (1980) and Linton & Evans (1993):

https://doi.org/10.1017/jfm.2026.11904 Published online by Cambridge University Press

$$b(\omega) = \frac{2\rho g L c_g(\omega)}{\omega^2} \sum_n \frac{\cos(\theta_n(\omega))}{\varepsilon_n} \left| \frac{\hat{\eta}_n^{(11)}(\omega)}{\hat{\zeta}(\omega)} \right|^2,$$
$$\varepsilon_n = \begin{cases} 1, & n = 0, \\ 2, & n \geq 1, \end{cases} \quad \theta_n(\omega) = \arcsin\left(\frac{2n\pi}{k(\omega)\, L}\right), \tag{5.1}$$

where b is the radiation damping, ω is the angular frequency, ρ is the water density, g is the gravitational acceleration, c_g is the group velocity, n is the symmetric mode number, k is the wavenumber, $\hat{\eta}_n^{(11)}$ is the complex amplitude of the linear radiated free surface in the nth channel mode propagating at angles $\pm\theta_n$, and $\hat{\zeta}$ is the complex amplitude of the body displacement. Thus the radiation damping can be computed in modal components and compared to the total (directly from Hydrostar) and checked for consistency, thus validating the modal decomposition.

6. The volume flow radiation model

Work on fluids is generally governed by volume flow and pressure. In an attempt to approximately account for the nonlinearities observed in the experimental data, we consider the volume flow in and out of the fluid due to the relative motion between body and fluid surface rather than the body heave motion itself. It is our hope that such a change of variables, partly inspired by small-body theory, may be used to extend the applicability of the linear potential flow solution for the problem at hand.

Accordingly, a partially nonlinear heave radiation model based on volume flow is now derived to model the observed nonlinear changes. We start from the time-domain formulation for the linear radiation potential (e.g. McIver & McIver 2011):

$$\phi^{(11)}(\boldsymbol{x}, t) = \Omega(\boldsymbol{x})\, \ddot{\zeta}(t) + \int_0^t K(\boldsymbol{x}, t-\tau)\, \dot{\zeta}(\tau)\, \mathrm{d}\tau, \tag{6.1}$$

where Ω is the infinite-frequency radiation potential, K is the heave radiation impulse response function for the potential, and the accents $\dot{\square}$ and $\ddot{\square}$ represent the conventional time derivatives. Heaving bodies are associated with oscillatory volume flow and radiated waves. In the classical literature for a heaving sphere (in open water, Havelock 1955; Hulme 1982) this link is clear, in that the radiated field far from the body is directly proportional to the strength of the wave source term used in constructing the solution. We propose to scale the radiated potential using the ratio of the instantaneous nonlinear volume flux associated with the sphere's immersed volume to the version from linear theory. Taking (6.1) and multiplying and dividing by the equilibrium waterplane area S_0 gives

$$\phi^{(11)}(\boldsymbol{x}, t) = \frac{1}{S_0}\Omega(\boldsymbol{x})\, [S_0\, \ddot{\zeta}(t)] + \frac{1}{S_0}\int_0^t K(\boldsymbol{x}, t-\tau)\, [S_0\, \dot{\zeta}(\tau)]\, \mathrm{d}\tau, \tag{6.2}$$

and 'correcting' the products $S_0\, \ddot{\zeta}(t)$ and $S_0\, \dot{\zeta}(\tau)$ to the time derivatives of the exact nonlinear submerged volume (as discussed in § 2), we obtain the partially nonlinear model

$$\phi(\boldsymbol{x}, t) = -\frac{1}{S_0}\left(\Omega(\boldsymbol{x})\, \ddot{V}(t) + \int_0^t K(\boldsymbol{x}, t-\tau)\, \dot{V}(\tau)\, \mathrm{d}\tau\right). \tag{6.3}$$

The free-surface elevation can be computed using the linear free-surface boundary condition

$$\eta(t) = -\frac{1}{g}\frac{\partial \phi}{\partial t}\bigg|_{z=0}, \tag{6.4}$$

https://doi.org/10.1017/jfm.2026.11904 Published online by Cambridge University Press

in which case the first term of (6.3) does not enter. This volume flow model is consistent with the local nonlinearity at the body being of greater importance than the nonlinearity associated with the free-surface boundary condition, similar to body-exact models noted earlier. In contrast to those models, however, this method does not enforce satisfaction of the body boundary condition. Due to the complexity of the far-field solution in a channel (discussed in § 5), construction of the kernel K is unappealing in this case (as also noted by Cohen & Troesch (1988) for the case of a sphere in a channel). Using the Fourier transform of the nonlinear volume flux time series, an equivalent calculation can be carried out in the frequency domain using the free-surface transfer functions shown in figure 3. The volume flow model is physically intuitive, with smaller radiated waves generated when the volume flux is smaller than its prismatic approximation, and vice versa.

For a heaving sphere with an initial draft of one radius (i.e. nominally half-immersed), the submerged volume (beneath the still free surface) is

$$V(t) = \frac{1}{3}\pi\Big(2R^3 - 3R^2\,\zeta(t) + \zeta^3(t)\Big), \tag{6.5}$$

where R is the radius of the sphere. We note that this expression holds for any heave displacement time series $\zeta(t)$, including the specific 'focused' signals ζ_ψ used in this work. With such an analytical expression in hand, there is essentially no extra computational cost in using the volume flow model compared to the linear. Importantly, since (6.5) only contains first- and third-order terms, the proposed nonlinear model (with contributions proportional to $\dot{V}$) yields only these terms. No even-ordered terms are produced due to the even geometry about the waterline. In fact, one can further refine the model to only simulate the first-harmonic terms (i.e. removing the third-harmonic $\eta^{(33)}(t)$ terms) by making the substitution $\zeta^3(t) \to (3/4)\,\zeta(t)\,[\zeta^2(t) + H(\zeta(t))^2]$ in (6.5), where H is the Hilbert transform operator (as per Walker *et al.* 2004). This allows the model to be directly compared with the experimentally extracted first-harmonic data. Another useful observation is the opposing signs of the first- and third-order terms, which would reduce the amplitude scaling of the first harmonic to be slightly less than linear, consistent with the results shown. Due to manufacturing limitations, our spherical model is very slightly elongated vertically ($R_z/R_x = 1.008$), but a spheroidal volume also shares the same equations (down to some constants), thus all of the traits discussed above are valid.

7. Comparison and discussion

Experimental 'added mass' and 'radiation damping' coefficients are now derived in the conventional manner using the total first-harmonic force

$$\tilde{m}(\omega) = \frac{1}{\omega^2}\,\mathrm{Re}\left(\frac{\hat{F}^{(1)}(\omega)}{\hat{\zeta}(\omega)}\right), \quad \tilde{b}(\omega) = -\frac{1}{\omega}\,\mathrm{Im}\left(\frac{\hat{F}^{(1)}(\omega)}{\hat{\zeta}(\omega)}\right), \tag{7.1}$$

where the $\tilde{\square}$ accent is used to differentiate them from the theoretical added mass m and radiation damping b calculated from linear theory. This distinction is important, because the experimental ratios presented cannot be used in the same way as the linear coefficients: they are functions of the spectral shape and amplitude of the input signal. The experimental values are plotted in figure 4 with the same colouring conventions as in figure 2. Additionally, we also plot the linear result in dotted and bold solid lines, where the dotted lines are the direct frequency-domain calculations from Hydrostar (2016) (thus assuming a steady-state system), and the bold solid lines are processed in the same way as the experimental data, i.e. a time series truncated to the same duration (prior to

https://doi.org/10.1017/jfm.2026.11904 Published online by Cambridge University Press

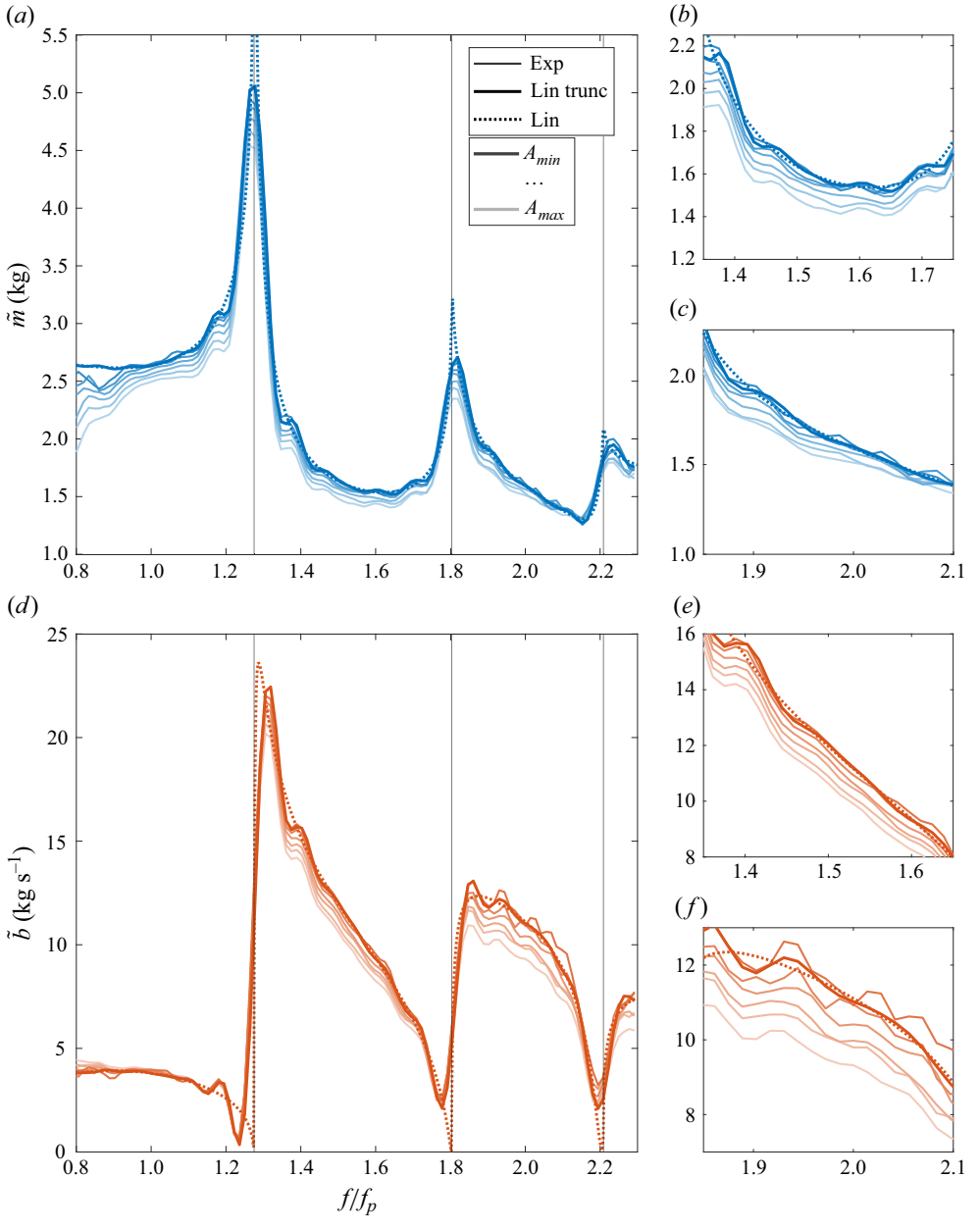


Figure 4. Experimental (*a–c*) 'added mass' and (*d–f*) 'radiation damping' coefficients for six input motion amplitudes, where the darker lines represent the smaller input motion amplitudes. Thin solid lines are the experimental data calculated from (7.1). Dotted lines are results from linear potential flow theory calculated from Hydrostar (2016). Bold solid lines are also from linear potential flow theory, truncated in the same way as the experimental data. Thin black vertical lines are cut-off frequencies. The smaller plots are used to better show regions of interest. Peak frequency of the motion input is $f_p = 0.8$ Hz.

experimental reflections), and then transformed to the frequency domain via a Fourier transform. The thin vertical black lines are the cut-off frequencies described in § 5, where the effects of channel modes are discussed. The smaller plots provide magnified views for regions of interest.

https://doi.org/10.1017/jfm.2026.11904 Published online by Cambridge University Press

Naturally, the progressive reductions in the amplitude-normalised responses observed in the time series in figure 2 are also apparent in the frequency domain, where the 'transfer functions' appear to gradually reduce with increasing input motion amplitudes. Additionally, the smallest amplitude lines appear to be consistent with the theoretical linear results calculated from Hydrostar, as expected. The reductions in both added mass and damping are in contrast to the body-exact computations of Lin & Yue (1991) where the 'added mass' was found to decrease considerably, while the 'damping' remained close to constant. However, those results were only for a single monochromatic motion input (at a frequency of approximately $1.75\,f_p$ here).

Figure 5 shows the ratio of the first-harmonic amplitudes of the radiated free surface and body displacement. In addition to the experimental and linear potential flow theory curves, results from the volume flow model are displayed. The model appears to effectively capture the nonlinearity in the radiated waves, both in the near field (figures 5(*a–c*), green colour) and in the far field (figures 5(*d–f*), purple colour), corresponding to wave gauges 7 and 8, respectively, in figure 1. These observations largely hold true for the other peak frequencies shown in Appendix A.

Before discussing these results in more detail, we note some discrepancies between the experimental and numerical radiated free-surface amplitudes in the form of oscillations seen in the low-frequency tails of the experimental data in figure 5. These are due to reflections of the radiated wave from either the wavemaker or the beach, and therefore do not appear in the numerical data, which are simulated assuming a channel of infinite length. The time series used to generate these plots are thus truncated early to minimise the impact of these reflections, but ultimately a compromise is required since we also try to retain as much of the true behaviour as possible. This is further exacerbated in the lower peak frequencies (shown in Appendix A) where the waves travel even faster and more reflections inevitably contaminate the results, incurring larger spurious oscillations (especially in the far-field wave gauge 8).

One of the notable features of the observed nonlinear behaviour is that the amplitude separations are more pronounced at the high-frequency tails, which was also observed and discussed in Tan *et al.* (2025). The nonlinear terms present, in addition to their different amplitude scaling properties, also possess broader bandwidths than the linear term, a property known as 'spectral smearing' (Fitzgerald *et al.* 2014), caused by the sum–frequency and difference–frequency interactions. For example, given a linear term with frequency content that spans $0.6\,f_p$ to $2.5\,f_p$, the third-order response from the $(++-)$ frequency interaction will span from 0 to $4.4\,f_p$. As a result of this difference in bandwidths, the first-harmonic $F^{(11)} + F^{(31)}$ is usually dominated by the linear term $F^{(11)}$ around the peak frequency where most of its energy is concentrated. However, the linear term $F^{(11)}$ subsides more rapidly than the third-order term $F^{(31)}$ towards the tails of the spectrum, therefore the first-harmonic lines deviate more from the linear prediction as the nonlinear contribution grows larger. This effect is, by nature, limited to broad-banded inputs, thus the influence of these terms is much more difficult to observe in monochromatic inputs (such as those used by Vantorre 1986*b*). The free surface (experimental and numerical) and the 'radiation damping' results exhibit this spectral smearing property, while the experimental 'added mass' appears to be the sole exception. Since radiation damping and the far-field radiated free surface are directly linked, it is encouraging to see analogous nonlinear behaviour in these two quantities.

Added mass, on the other hand, is dominated by local effects and is more sensitive to experimental uncertainties. One of these uncertainties is the removal of the hydrostatic force discussed in § 3. While every care was taken to estimate the volume of the model as

https://doi.org/10.1017/jfm.2026.11904 Published online by Cambridge University Press

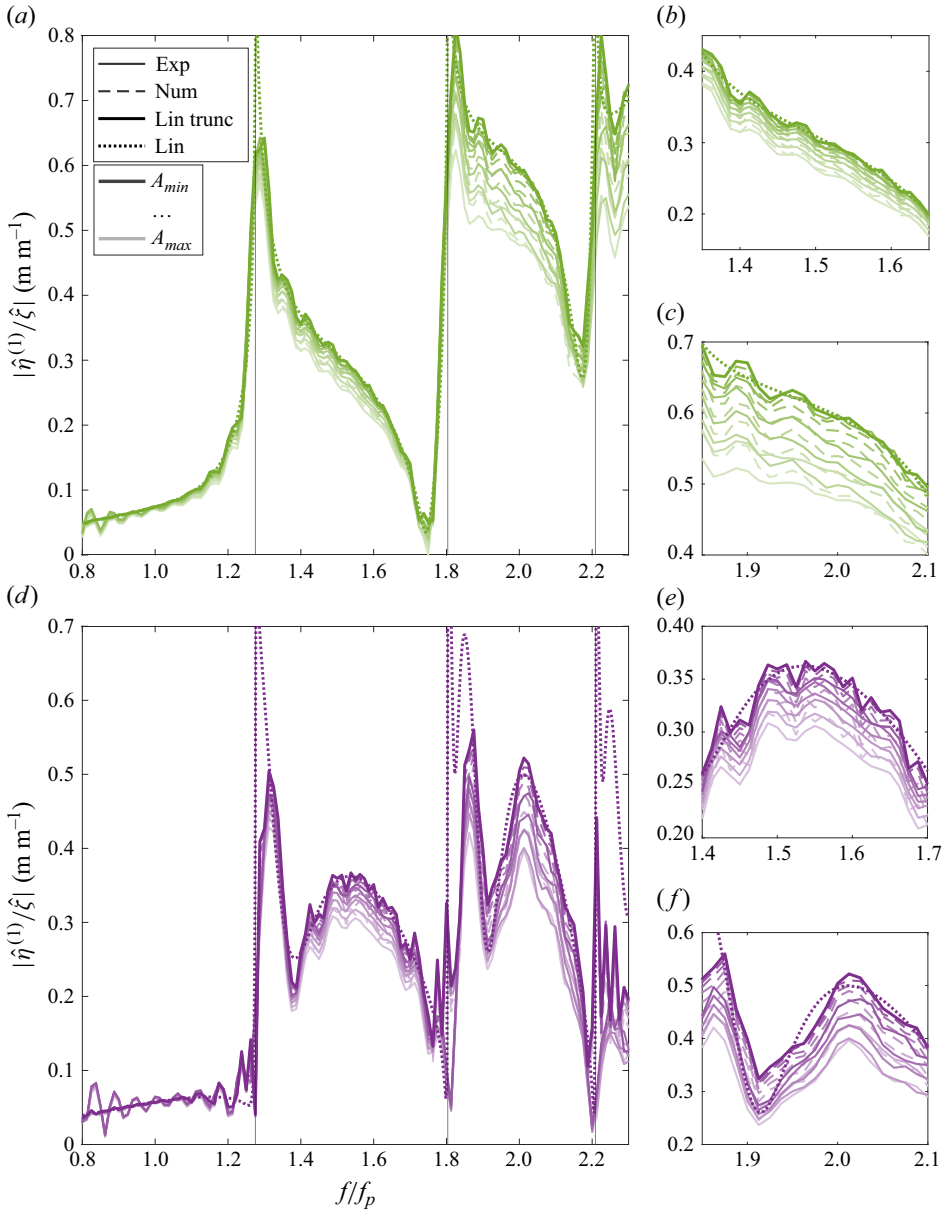


Figure 5. Ratio of the first-harmonic amplitudes of the radiated free surface and body displacement for wave gauges (*a–c*) 7 and (*d–f*) 8 for six input motion amplitudes, where the darker lines represent the smaller input motion amplitudes. Thin solid lines are the experimental data. Thin dashed lines are derived from the nonlinear numerical volume flow model derived in § 6. Dotted lines are results from linear potential flow theory calculated from Hydrostar (2016). Bold solid lines are also from linear potential flow theory, truncated the same way as in the experimental data. Thin black vertical lines are cut-off frequencies. The smaller plots are used to better show regions of interest. Peak frequency of the motion input is $f_p = 0.8$ Hz.

accurately as possible, small local defects due to the manufacturing method made this very challenging, even with the three-dimensional scan. It is apparent that the experimental 'added mass' estimates exhibit different trends in amplitude change as a function of

https://doi.org/10.1017/jfm.2026.11904 Published online by Cambridge University Press

frequency compared to the other results. Unfortunately, the Kramers–Kronig relations assume a linear system, so cannot be used on the nonlinear quantities studied here.

Since the observed nonlinear changes in the radiated wave data are largely consistent with the volume flow model (which only contains a cubic nonlinear term), this implies that these effects are caused by the third-order first-harmonic $F^{(31)}$ and $\eta^{(31)}$ terms, as initially proposed. While there is a method to estimate the order of the nonlinear terms from the amplitude scaling of the experimental data, as shown in Tan *et al.* (2025), we do not use it here since the smaller amplitude cases are somewhat noisy.

While we have considered that viscous effects potentially contribute to the observed nonlinearities, due to the small size of the spherical model and low Keulegan–Carpenter number ($KC < 2.1$) it is likely that the boundary layer is laminar and does not separate. This is known to linearly affect the added mass and radiation damping (Stokes 1851; Molin & Etienne 2000), and thus would manifest in the frequency-domain plots (figures 4 and 5) as a single line offset from the linear potential flow solution, as opposed to the systematic separation of lines observed. We also estimate the magnitude of the laminar drag force later, in § 8, and find that this viscous force is approximately 0.5 % of the measured force at most.

The lower peak frequencies in Appendix A show similar nonlinear behaviours, where the ordered reductions in the 'transfer functions' can be observed clearly for the 0.6 Hz results. While the 0.4 Hz results (with correspondingly smaller hydrodynamic forces) are more corrupted by noise, they also show a general decreasing trend with increasing motion amplitude. Interestingly, the volume flow model appears effective in modelling the radiation behaviour at all peak frequencies, suggesting that the volume corrections are the dominant source of nonlinearity across the tested frequency range. Therefore, while there are different features in the transfer functions across the peak frequencies (largely influenced by the channel modes discussed in § 5), the nonlinearities appear to be largely independent of the peak frequency, depending only on the instantaneous submerged volume.

We now briefly mention some wider implications of these results. Since the volume flow model is an extremely simple model to implement, only requiring the linear hydrodynamic coefficients and basic geometric parameters (the equilibrium waterplane area and instantaneous submerged volume), it can be evaluated almost instantly and could ultimately be used in real-time control of WECs. In fact, if we inspect the linear equation (6.1) and the volume flow nonlinear equation (6.3), then there is practically no extra computational cost if the submerged volume can be directly obtained from the draft.

We note that spherical or near-spherical geometries, as studied here, excite these third-order wave-structure interactions particularly strongly given the cubic relationship between their draft and submerged volume. As such geometries are common in point absorber designs, the effects are worthy of study.

8. Near- and far-field radiated power

To further test the consistency of the measurements, we also compare the input power in the near field (transferred from the moving body to the fluid), and the radiated power in the far field (transported by the radiated waves). Since the nonlinearities appear most strongly in the high-frequency tail, we focus on the frequency band from $1.4\,f_p$ to $1.7\,f_p$ between the first and second cut-off frequencies (avoiding frequencies very close to the cut-offs due to the extremely slow propagation of the nearly trapped waves).

Two factors prevent simply using the measured radiated free-surface measurements directly. First, the inline propagating mode ($n = 0$) and the obliquely propagating channel

https://doi.org/10.1017/jfm.2026.11904 Published online by Cambridge University Press

mode ($n = 1$) must be explicitly separated since they have different relationships between modal amplitudes and power, which need to be accounted for when calculating the transported power. Second, dissipation of energy during propagation from the body to the far-field gauge should be accounted for. To separate the total measured wave elevation into modes, we therefore fit to the following basic equation, which exploits the inline propagation speed of each mode to differentiate their contributions:

$$\hat{\eta}^{(1)}(\omega, x) = \sum_{n=0,1} \hat{\eta}_n^{(1)}(\omega, x_0) \exp\left[(-\mathrm{i}\, k(\omega) \cos\left(\theta_n(\omega)\right) - \alpha_n(\omega)\right)(x - x_0)], \tag{8.1}$$

where x_0 is a reference point, and α_n is the (complex) dissipation coefficient of the nth mode accounting for laminar boundary layer friction on the flume walls and free surface (discussed later and derived in Appendix B). This fitting procedure therefore takes the measured wave elevation from several inline wave gauges and, at each frequency, finds the best-fit complex amplitudes $\hat{\eta}_0^{(1)}$ and $\hat{\eta}_1^{(1)}$. This approach (including only linear dispersion with laminar dissipation) is appropriate if $k\delta \gg (ka)^2$, where $\delta = (\nu/\omega)^{1/2}$, and a is a representative wave amplitude (Mei & Liu 1973). Here, the largest total wave elevation measured anywhere in the flume (for the largest motion amplitude) was 9 mm (figure 2) – yielding $(k_p \eta_{max}^{(1)})^2 = 6 \times 10^{-4}$, while $k_p\delta = 1 \times 10^{-3}$. Given that this is the largest free-surface elevation measured (close to the body) for the largest body motion, and that the groups disperse rapidly with distance, this is a reasonable assumption. We note in passing that if transverse measurements of the far-field free-surface were available at a single distance, then one could fit the $n = 1$ mode profile since the $n = 0$ mode is flat across the channel (as done in § 5 for the theoretical linear results). However, the wave gauge layout in our tests did not contain transversely positioned gauges in the far field (see figure 1).

Figure 6 shows the measured free-surface time series from the four far-field wave gauges used for the fitting, which clearly demonstrates the different propagation speeds of the two modes, and their progressive separation from wave gauges 8–11. The shaded regions show the range of propagation speeds accounting for frequency dispersion and the dispersion due to the different propagation angles in the $n = 1$ group. Wave gauge 12 is not used for this analysis since it is very close to the beach, and the uncompromised time window is too short. After truncating the reflections and using a conventional least squares fitting method, the separated wave elevations at each gauge were obtained, and plotted for wave gauge 8 in figure 7 for all six input motion amplitudes, alongside a linear solution that was processed identically (i.e. accounting for the laminar dissipation over the distance from the sphere to wave gauge 8, and using the same truncations).

The fitted $n = 0$ and $n = 1$ modes appear to be consistent with the linear solution, suggesting that the separation method is effective. The fitting was substantially improved by including the dissipation coefficient from side walls only, which reduced the root mean square error between the fitted and measured total amplitude by approximately 40 %. (Friction from the bottom of the flume is negligible as the waves in this frequency band are on deep water.) However, the observed dissipation rate was still noticeably higher, so we also included dissipation at the free surface, which is affected by surface contamination and 'ageing' effects commonly experienced in laboratory tank tests (Van Dorn 1966; Mei 1989). This free-surface dissipation coefficient was scaled by a single factor β, common to all frequencies, between 0 (no contamination) and 1 (inextensible film present) to best fit the measurements, as noted in Appendix B. The final value used was $\beta = 0.31$, which reduced the error by a further 55 %. With the amplitudes for each mode now separated, we can perform the power calculation using the far-field radiated waves, and compare it to the results in the near field.

https://doi.org/10.1017/jfm.2026.11904 Published online by Cambridge University Press

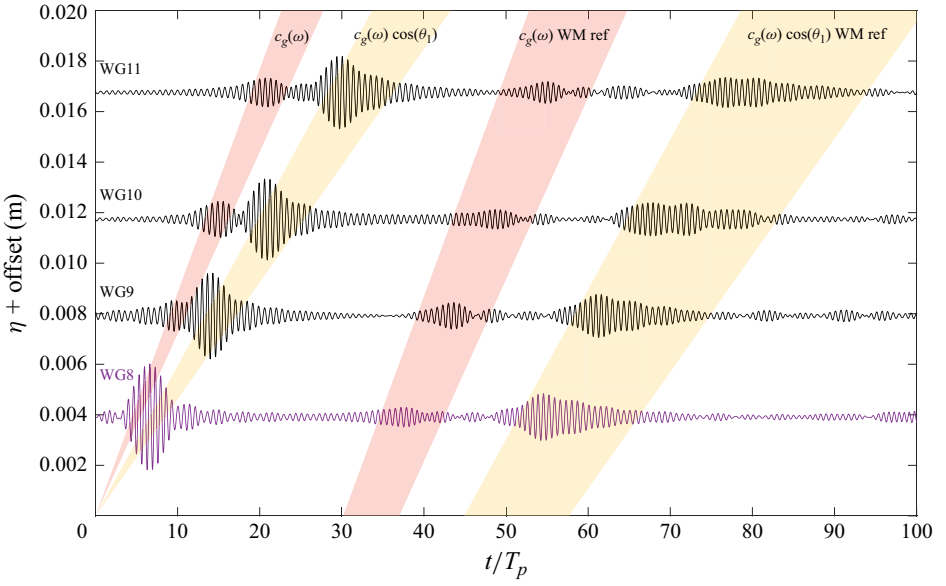


Figure 6. Extended experimental first-harmonic wave elevation time series for $A = 0.07$ m and $f_p = 0.8$ Hz across wave gauges (WG) 8–11 (see figure 1), band-pass filtered from $f_l/f_p = 1.4$ to $f_u/f_p = 1.7$. Vertical axis offsets for each gauge are proportional to their respective x locations in the flume. The shaded regions show the dispersion of the radiated wave group accounting for both frequency and propagation angle of all components. For completeness, waves radiated from the sphere in the $-x$ direction, and subsequently reflected from the wavemaker (WM), are also shown.

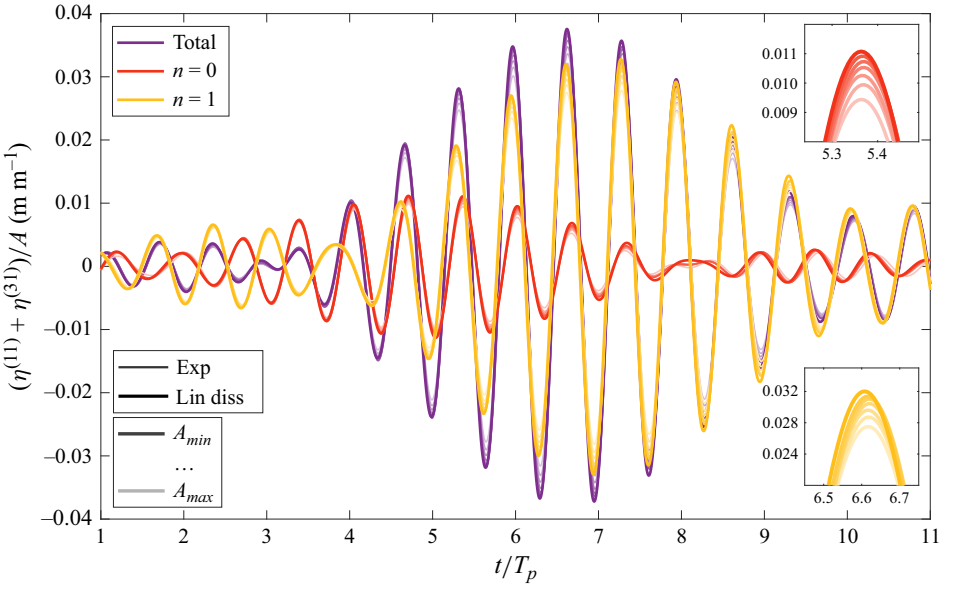


Figure 7. Filtered ($1.4\,f_p$ to $1.7\,f_p$) and amplitude-normalised first-harmonic wave elevation time series for $f_p = 0.8$ Hz from wave gauge 8 decomposed into the $n = 0$ and $n = 1$ modes through fitting the experimental data to (8.1). Six amplitudes are shown, where the darker lines represent the smaller input motion amplitudes. The thin lines are the experimental data, and the bold line is the corresponding linear solution for the radiated field from the sphere, with linear dissipation applied. Inset plots show magnified views of regions of interest.

https://doi.org/10.1017/jfm.2026.11904 Published online by Cambridge University Press

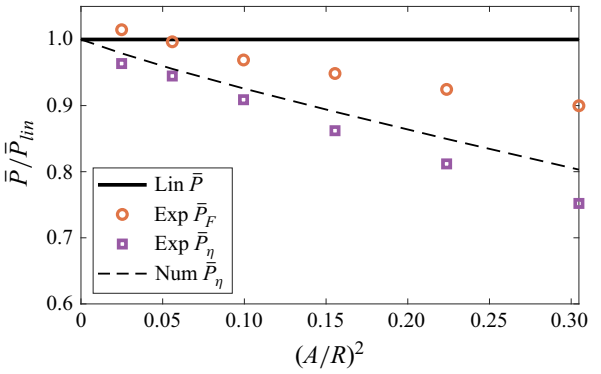


Figure 8. Experimental (circle and square markers), volume flow numerical (dashed black line) and linear (solid black line) mean power from the near-field (orange) and far-field (purple) calculations over the frequency band from $1.4\,f_p$ to $1.7\,f_p$. Linear viscous effects have been removed from the experimental data as described in the text. The vertical axis is normalised by the power from linear theory.

The nonlinear input mean power in the near field $\overline{P}_F$ follows from the product of the experimental force and velocity summed over the frequencies present in our band of interest:

$$\overline{P}_F = \frac{1}{2}\sum_i \mathrm{Re}\left(\mathrm{i}\omega_i\,\hat{\zeta}(\omega_i)\,\hat{F}^{*(1)}(\omega_i)\right), \tag{8.2}$$

where $\square^*$ denotes the complex conjugate. Consistent with (5.1), for the radiated waves we obtain

$$\overline{P}_\eta = \rho g L \sum_i c_g(\omega_i) \sum_n \frac{\cos\left(\theta_n(\omega_i)\right)}{\varepsilon_n}\left|\hat{\eta}_n^{(1)}(\omega_i, 0)\right|^2, \tag{8.3}$$

where $\overline{P}_\eta$ represents the mean power calculated from the (far-field) wave elevation measurements. Note that in the above, the mode amplitudes $\hat{\eta}_n^{(1)}$ are taken at the sphere location (i.e. at $x = 0$, using (8.1)) such that the dissipation does not contaminate the far-field power estimate. We also note that in both of the above expressions for mean power estimates, only products of the same frequency terms are needed, as any other terms would be oscillatory in nature and therefore not contribute to the time-averaged value.

We also attempted to remove the laminar drag force on the body from the experimental result to achieve a more accurate comparison to the numerical potential flow results. If we assume that the boundary layer thickness is much smaller than the body radius, and thus the body surface can be locally treated as a flat plate, then we can use the classical solution from Stokes' oscillating plate to estimate the shear stress. This is calculated for 65 discretised area elements over the hemisphere, using the local tangential velocities calculated from Hydrostar, and then integrated to obtain the total laminar drag. Consistent with Stokes (1851) and Molin & Etienne (2000), this force was linear and at $\pi/4$ phase to the displacement. The magnitude was, however, extremely small (less than 0.5 % of the measured force), and thus hardly made a difference.

Using (8.2) and (8.3) on the linear and experimental data, and (8.3) on the volume flow numerical data, then gives figure 8, which shows the mean power in the near and far fields across the range of tested displacement amplitudes. The vertical axis is normalised by the linear power. The nonlinear changes in power are not the same in the near- and far-field results, with the power in the near field registering smaller changes with amplitude than in

https://doi.org/10.1017/jfm.2026.11904 Published online by Cambridge University Press

the far field, and a small offset between the smallest amplitudes. The offset is suggestive of additional linear damping, and the slightly different shapes of the curves are possibly indicative of quadratic drag – effects that could increase the near-field power but decrease the far-field power. Nevertheless, a systematic, monotonic decrease in radiated power is observed in all curves, with the dominant trend appearing to be proportional to $(A/R)^2$, as would be expected as the leading-order effect of a third-order contribution. The volume flow model gives a reasonable match to the far-field data.

9. Conclusions

An experimental campaign involving radiation tests in a wave flume was conducted, with a spherical model actuated in heave to investigate the nonlinear first-harmonic radiation forces and radiated waves. Several motion amplitudes and three peak frequencies of broad-banded group signals were tested. Accurate measurements of inertia and hydrostatic force were used to isolate the radiation forces, with phase combinations used to isolate the first harmonics. The range of amplitudes then allowed identification of nonlinear effects. These effects were shown as progressive reductions in both the time- and frequency-domain representations of the first-harmonic responses, as the motion amplitude increased. The peak first-harmonic radiation force was found to be $\sim 10\,\%$ lower than linear predictions when the motion amplitudes were approximately half the sphere radius, with corresponding reductions in the 'added mass' and 'radiation damping' coefficients. The radiated free-surface from near- and far-field wave gauges also showed the same nonlinear pattern, decreasing progressively with amplitude.

Based on their occurrence in the phase-separated odd harmonic, the observed nonlinearities were attributed to third-order first-harmonic terms. The possibility that viscous drag could instead cause these changes was considered; however, given the low Keulegan–Carpenter number and the small spherical geometry, it was reasoned that these effects would primarily be linear and thus would not cause the observed nonlinear changes.

A simple partially nonlinear volume flow radiation model was proposed, based on using the instantaneous rate of change of submerged volume. The nonlinear trends predicted by the model showed reasonably close agreement with the experimental data for the radiated waves, in both near and far fields. While linear theory was found to be remarkably effective for this system overall, the observed first-harmonic nonlinearities were nonetheless modelled well by this volume flow radiation model.

Near- and far-field estimates of radiated power in a frequency band of interest were derived from the experimental results, with the results exhibiting systematic reductions in radiated power with amplitude. These results have fundamental implications for WECs, where the connection of the far-field radiated waves to absorbed power has long been recognised (Falnes & Kurniawan 2020).

These experiments form a part of a larger campaign investigating novel methods to identify, extract and model nonlinear terms in resonant WECs, and we are currently working to extend this to combined tests where both incident waves and prescribed motions are applied simultaneously.

Funding. This work is funded by the ARC (LP210100397;DP250104899), a UWA Research Impact Grant, and the Blue Economy Cooperative Research Centre CRC-20180101. B.T. is supported by the Australian Government RTP at UWA. A.K. is supported by MERA, jointly funded by UWA and the Western Australian Government. The authors acknowledge stimulating discussions with Professor P.H. Taylor. Provision of the scanner by TechWorks (https://futurelabatuwa.com.au/tech-works/) at UWA is gratefully acknowledged.

Declaration of interests. The authors report no conflict of interest.

https://doi.org/10.1017/jfm.2026.11904 Published online by Cambridge University Press

Appendix A. Additional plots for the lower peak frequencies

See figures 9, 10, 11 and 12.

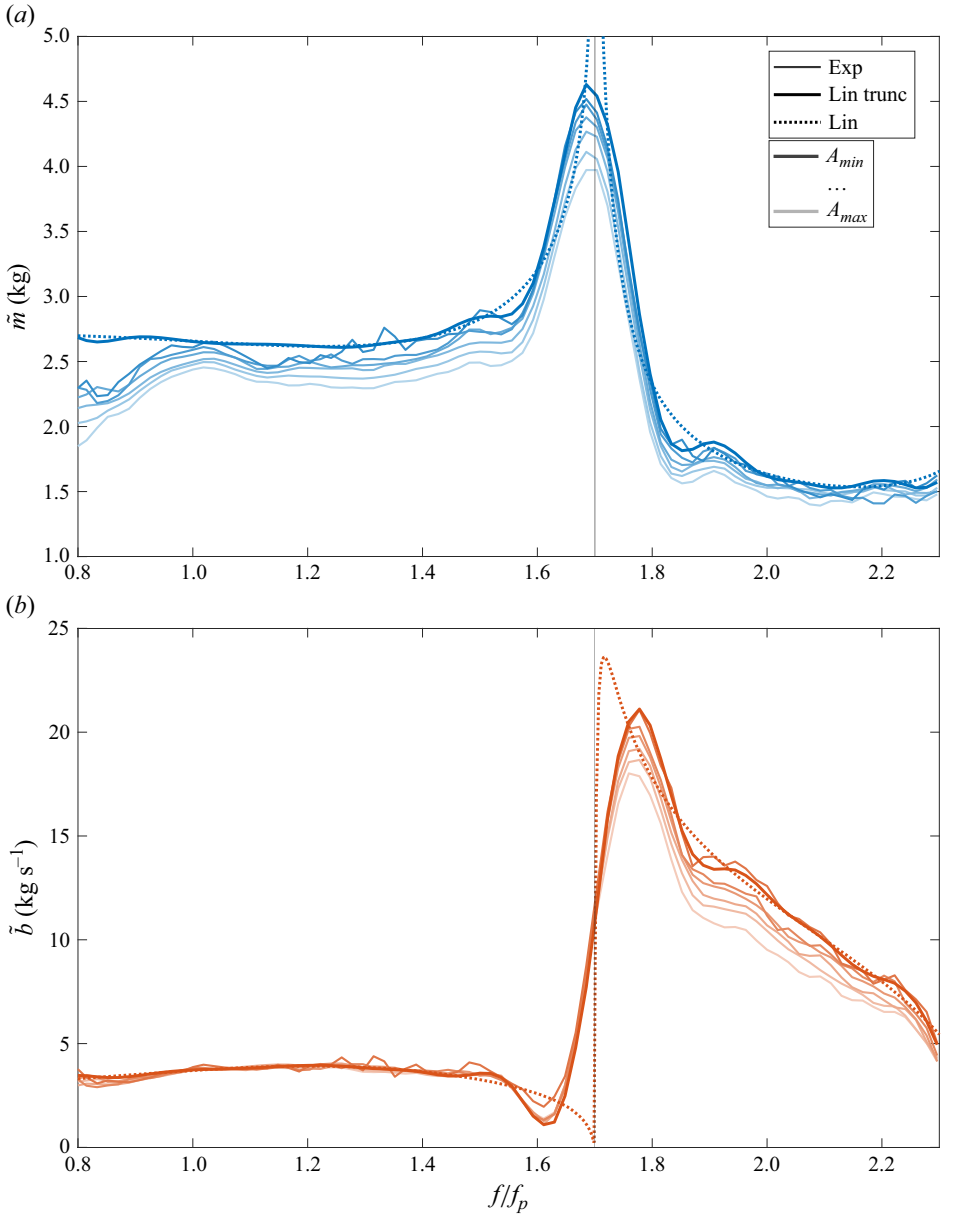


Figure 9. Experimental (*a*) 'added mass' and (*b*) 'radiation damping' coefficients for six input motion amplitudes, where the darker lines represent the smaller input motion amplitudes. Thin solid lines are the experimental data calculated from (7.1). Dotted lines are results from linear potential flow theory calculated from Hydrostar (2016). Bold solid lines are also from linear potential flow theory, truncated in the same way as the experimental data. Thin black vertical lines are cut-off frequencies. Peak frequency of the motion input is $f_p = 0.6$ Hz.

https://doi.org/10.1017/jfm.2026.11904 Published online by Cambridge University Press

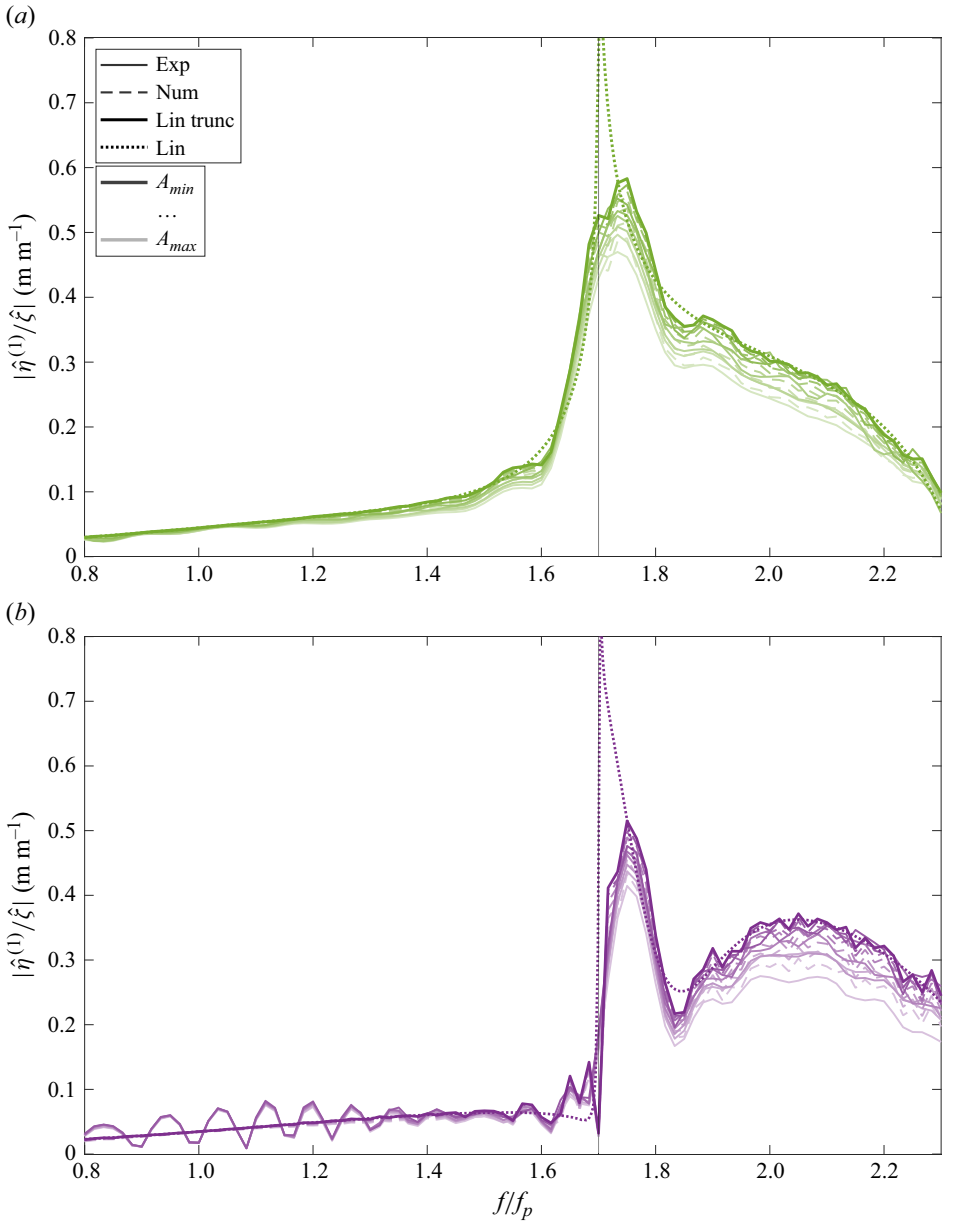


Figure 10. Ratio of the first-harmonic amplitudes of the radiated free surface and body displacement for wave gauges (*a*) 7 and (*b*) 8, for six input motion amplitudes, where the darker lines represent the smaller input motion amplitudes. Thin solid lines are the experimental data. Thin dashed lines are derived from the nonlinear numerical volume flow model derived in § 6. Dotted lines are results from linear potential flow theory calculated from Hydrostar (2016). Bold solid lines are also from linear potential flow theory, truncated in the same way as the experimental data. Thin black vertical lines are cut-off frequencies. Peak frequency of the motion input is $f_p = 0.6$ Hz.

https://doi.org/10.1017/jfm.2026.11904 Published online by Cambridge University Press

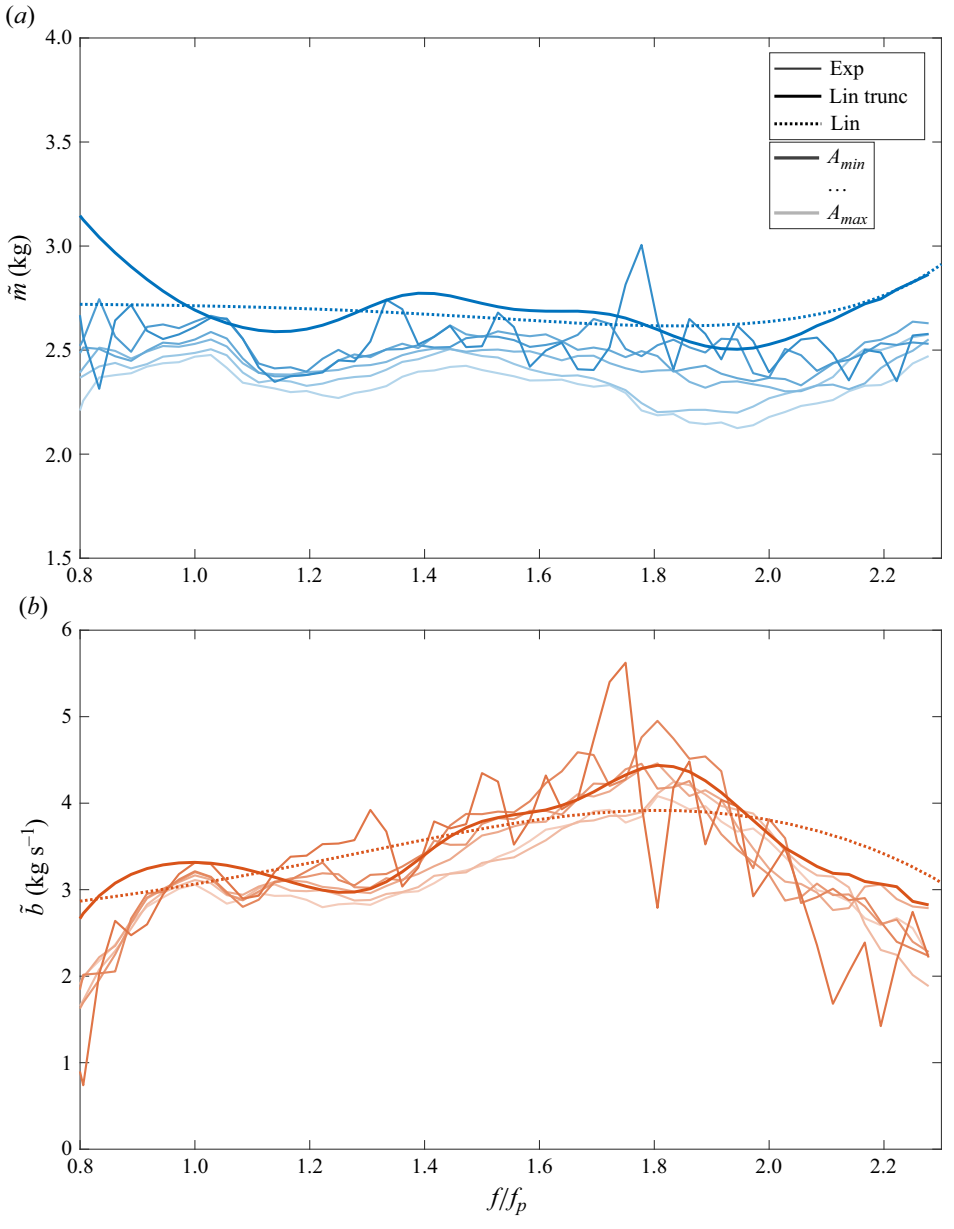


Figure 11. Experimental (*a*) 'added mass' and (*b*) 'radiation damping' coefficients for six input motion amplitudes, where the darker lines represent the smaller input motion amplitudes. Thin solid lines are the experimental data calculated from (7.1). Dotted lines are results from linear potential flow theory calculated from Hydrostar (2016). Bold solid lines are also from linear potential flow theory, truncated in the same way as the experimental data. Peak frequency of the motion input is $f_p = 0.4$ Hz.

https://doi.org/10.1017/jfm.2026.11904 Published online by Cambridge University Press

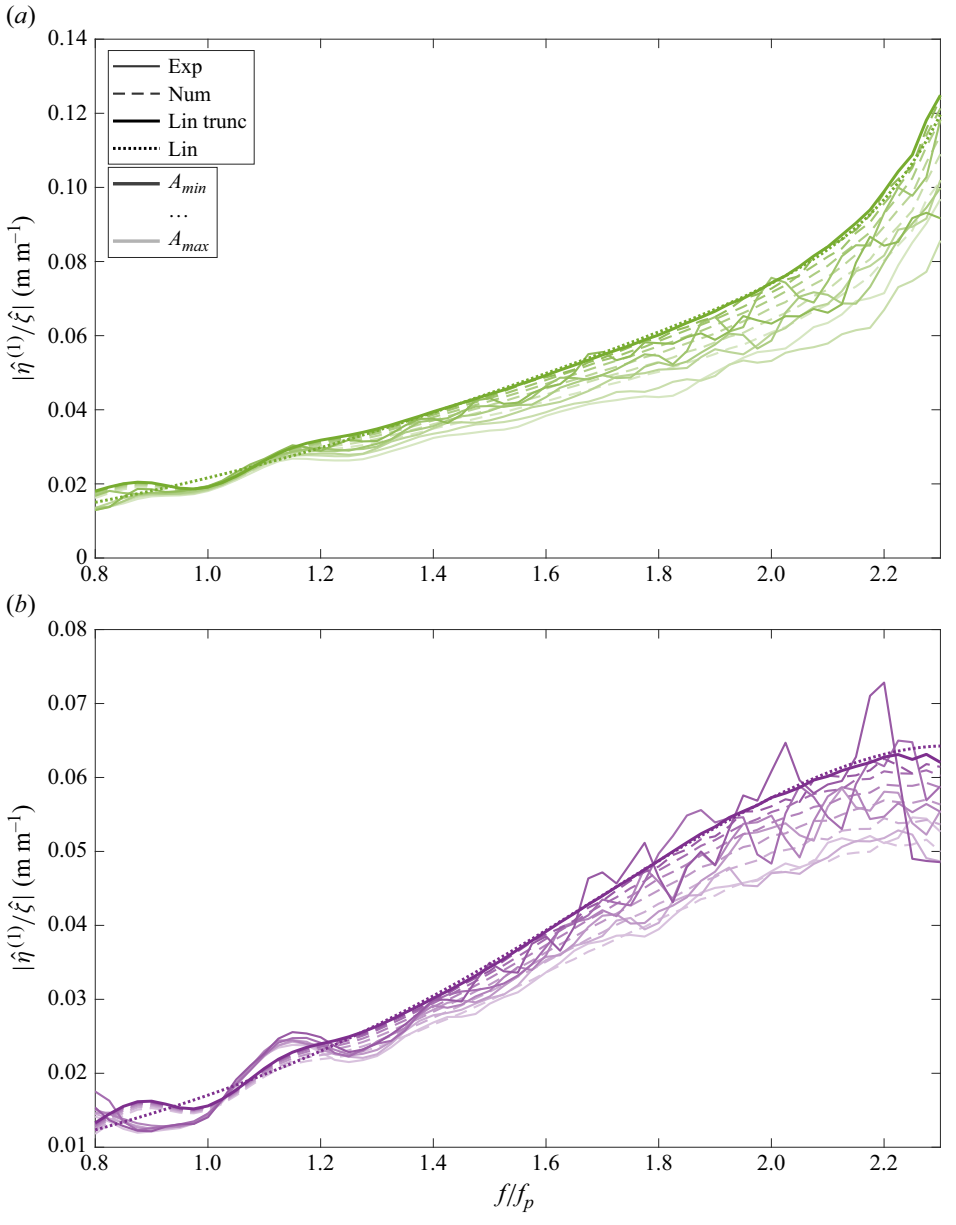


Figure 12. Ratio of the first-harmonic amplitudes of the radiated free surface and body displacement for wave gauges (*a*) 7 and (*b*) 8, for six input motion amplitudes, where the darker lines represent the smaller input motion amplitudes. Thin solid lines are the experimental data. Thin dashed lines are derived from the nonlinear numerical volume flow model derived in § 6. Dotted lines are results from linear potential flow theory calculated from Hydrostar (2016). Bold solid lines are also from linear potential flow theory, truncated in the same way as the experimental data. Peak frequency of the motion input is $f_p = 0.4$ Hz.

Appendix B. Viscous dissipation of radiated waves by channel walls and free surface

We seek to derive the radiated wave amplitude $A(x)$ as the wave propagates down the channel and gradually decays due to the viscous dissipation at the side walls and an unskimmed (inextensible) free surface for both flat ($n = 0$) and obliquely propagating

https://doi.org/10.1017/jfm.2026.11904 Published online by Cambridge University Press

channel modes ($n \geq 1$). The following equations are written assuming deep water and a single frequency for simplicity. Additionally, each channel mode is treated independently and, as such, interactions between the modes (at the same frequency) are neglected. Following the derivation in Keulegan (1959) and Molin *et al.* (2002) for laminar dissipation when $Re < 10^5$ (in our experiments, $Re < 1.3 \times 10^3$), the energy change over a unit surface per period is

$$\frac{\mathrm{d}E}{\mathrm{d}S} = -\pi\rho\sqrt{\frac{\nu}{2\omega}}u^2, \tag{B1}$$

where ν is the kinematic viscosity, and u is the total fluid velocity tangential to the boundary. At the vertical channel walls, the tangential velocity squared is given by

$$u^2_{n,wall} = \omega^2 \exp(2kz)\big(\cos^2(\theta_n) + 1\big)A_n^2, \tag{B2}$$

which accounts for the oblique propagation angle of the nth channel mode. Integrating over both channel walls then gives the energy dissipated by the walls over the longitudinal propagation distance:

$$\Delta E_{n,wall} = -\pi\rho g\sqrt{\frac{\nu}{2\omega}}\big(\cos^2(\theta_n) + 1\big)A_n^2\,\Delta x, \tag{B3}$$

which is consistent with Molin *et al.* (2002) for the plane wave where $\theta_0 = 0$. To account for the unskimmed free surface, which acts as a rigid, inextensible membrane to tangential flow, we evaluate the squared horizontal velocity at $z = 0$:

$$u^2_{n,surf} = \omega^2 A_n^2\big(\cos^2(\theta_n)\cos^2(k_y y) + \sin^2(\theta_n)\sin^2(k_y y)\big). \tag{B4}$$

Integrating this velocity across the channel width $y \in [-L/2, L/2]$ yields a geometric factor L/ε_n, producing the energy dissipated by the free surface:

$$\Delta E_{n,surf} = -\pi\rho\sqrt{\frac{\nu}{2\omega}}\left(\omega^2 A_n^2\frac{L}{\varepsilon_n}\right)\Delta x. \tag{B5}$$

Applying the deep-water dispersion relation ($\omega^2 = gk$), we can sum the wall and free-surface energy losses. Dividing by the period to get the total dissipated power, and considering an infinitesimal propagation length, gives

$$\frac{\mathrm{d}P_{n,diss}(x)}{\mathrm{d}x} = -\rho g\sqrt{\frac{\nu\omega}{8}}\left(\cos^2(\theta_n) + 1 + \frac{kL}{\varepsilon_n}\right)A_n^2(x). \tag{B6}$$

Now using the radiation damping given in (5.1) multiplied by $\omega^2|\hat{\zeta}|^2/4$ gives the radiated wave power for the $+x$ propagating wave:

$$P_{n,wave}(x) = \frac{1}{2}\rho g L c_g\left(\frac{\cos(\theta_n)}{\varepsilon_n}\right)A_n^2(x), \tag{B7}$$

which simplifies to the classical wave power expression $\rho g L c_g A_0^2/2$ for $n = 0$. Taking the spatial derivative

$$\frac{\mathrm{d}P_{n,wave}(x)}{\mathrm{d}x} = \rho g L c_g\left(\frac{\cos(\theta_n)}{\varepsilon_n}\right)A_n(x)\frac{\mathrm{d}A_n(x)}{\mathrm{d}x} \tag{B8}$$

https://doi.org/10.1017/jfm.2026.11904 Published online by Cambridge University Press

and equating with (B6) then gives

$$\frac{\mathrm{d}A_n(x)}{\mathrm{d}x} = -\alpha_n\, A_n(x),$$
$$\alpha_n = \frac{1}{gL}\sqrt{\frac{\nu\omega^3}{2}}\left(\frac{\varepsilon_n\left(\cos^2(\theta_n)+1\right)+kL}{\cos(\theta_n)}\right), \tag{B9}$$

with the corresponding solution

$$A_n(x) = A_n(0)\exp(-\alpha_n x), \tag{B10}$$

i.e. the amplitude of the nth mode decays exponentially at rate α_n as it propagates down the channel. The expression (B9) agrees with Ursell (1952) regarding the side wall contribution (after correcting for the missing factor of 2 in his original derivations), and with Hunt (1952) and Van Dorn (1966), who presented the $n=0$ expressions excluding and including the free-surface contribution, respectively. According to expression (B9), the $n \geq 1$ modes always decay faster down the channel than the $n=0$ mode at the same frequency. We note that when multiple channel modes are simultaneously present at frequencies above the first cut-off, the apparent dissipation rate of the total combined wave field becomes spatially varying. While the individual modal decay coefficients α_n remain constant, the cross-mode interference creates spatially variable velocity antinodes along the walls, resulting in a localised, non-uniform energy extraction that has been neglected here for simplicity.

In practice, we used a version of (B9) with two modifications. The first is to include an imaginary part equal in magnitude to the real part, as deduced by Mei & Liu (1973). The second is to add a fitting coefficient β in front of the free-surface term, as the full unskimmed surface dissipation was larger than indicated by measurements. Thus the final form is

$$\alpha_n = \frac{1+\mathrm{i}}{gL}\sqrt{\frac{\nu\omega^3}{2}}\left(\frac{\varepsilon_n\left(\cos^2(\theta_n)+1\right)+\beta kL}{\cos(\theta_n)}\right). \tag{B11}$$

References

Bai, W. & Eatock Taylor, R. 2006 Higher-order boundary element simulation of fully nonlinear wave radiation by oscillating vertical cylinders. *Appl. Ocean Res.* **28** (4), 247–265.

Chen, L.F., Zang, J., Taylor, P.H., Sun, L., Morgan, G.C.J., Grice, J., Orszaghova, J. & Tello Ruiz, M. 2018 An experimental decomposition of nonlinear forces on a surface-piercing column: Stokes-type expansions of the force harmonics. *J. Fluid Mech.* **848**, 42–77.

Cohen, S.B. & Troesch, A.W. 1988 The interaction of a floating body with vertical walls. *Intl Shipbuild. Prog.* **35** (401), 25–79.

Davidson, J. & Costello, R. 2020 Efficient nonlinear hydrodynamic models for wave energy converter design – a scoping study. *J. Mar. Sci. Engng* **8** (1), 35.

Dommermuth, D.G. & Yue, D.K.P. 1987 Numerical simulations of nonlinear axisymmetric flows with a free surface. *J. Fluid Mech.* **178**, 195–219.

Drake, K.R., Eatock Taylor, R., Taylor, P.H. & Bai, W. 2009 On the hydrodynamics of bobbing cones. *Ocean Engng* **36** (15), 1270–1277.

Falnes, J. & Kurniawan, A. 2020 *Ocean Waves and Oscillating Systems: Linear Interactions Including Wave-Energy Extraction*, Cambridge Ocean Technology Series, vol. 8. Cambridge University Press.

Faltinsen, O.M., Newman, J.N. & Vinje, T. 1995 Nonlinear wave loads on a slender vertical cylinder. *J. Fluid Mech.* **289**, 179–198.

Ferrant, P. 1991 A coupled time and frequency approach for nonlinear wave radiation. In *Eighteenth Symposium on Naval Hydrodynamics*, pp. 67–83. The National Academies Press.

https://doi.org/10.1017/jfm.2026.11904 Published online by Cambridge University Press

FITZGERALD, C.J., TAYLOR, P.H., EATOCK TAYLOR, R., GRICE, J. & ZANG, J. 2014 Phase manipulation and the harmonic components of ringing forces on a surface-piercing column. *Proc. R. Soc. A* **470** (2168), 20130847.

GU, H., STANSBY, P., STALLARD, T. & CARPINTERO MORENO, E. 2018 Drag, added mass and radiation damping of oscillating vertical cylindrical bodies in heave and surge in still water. *J. Fluids Struct.* **82**, 343–356.

HAN, S.Y., BOUSCASSE, B., LEROY, V., DELACROIX, S., GILLOTEAUX, JC., BONNEFOY, F. & LE TOUZÉ, D. 2024 Experimental study of hydrodynamic loads induced by the motion of a vertical circular cylinder with heave plates in proximity of the free surface. *Ocean Engng* **310**, 118712.

HAVELOCK, T.H. 1955 Waves due to a floating sphere making periodic heaving oscillations. *Proc. R. Soc. A* **231** (1184), 1–7.

HLOPHE, T., ADCOCK, T.A.A., DING, H., ZANG, J., DAI, S., TANG, T. & TAYLOR, P.H. 2025 Nonlinear wave loads on monopile foundations and structural response in severe wave conditions. *Appl. Ocean Res.* **164**, 104790.

HULME, A. 1982 The wave forces acting on a floating hemisphere undergoing forced periodic oscillations. *J. Fluid Mech.* **121**, 443–463.

HUNT, J.N. 1952 Viscous damping of waves over an inclined bed in a channel of finite width. *La Houille Blanche* **38** (6), 836–842.

Hydrostar 2016 Hydrostar for experts user manual. Bureau Veritas, 92571 Neuilly-Sur-Seine, version 7.3. Available at: https://www.scribd.com/document/432125438/nave-tehnice.

KASHIWAGI, M. 1989 3-D integral-equation method for calculating the effects of tank-wall interference on hydrodynamic forces acting on a ship. *J. Kansai Soc. Naval Architects Japan* **212**, 89–101.

KEULEGAN, G.H. 1959 Energy dissipation in standing waves in rectangular basins. *J. Fluid Mech.* **6** (1), 33–50.

KRAMER, M.B. *et al.* 2021 Highly accurate experimental heave decay tests with a floating sphere: a public benchmark dataset for model validation of fluid–structure interaction. *Energies* **14** (2), 269.

LIN, W.M. & YUE, D. 1991 Numerical solutions for large-amplitude ship motions in the time domain. In *Eighteenth Symposium on Naval Hydrodynamics*, pp. 41–65. The National Academies Press.

LINTON, C.M. & EVANS, D.V. 1993 Hydrodynamic characteristics of bodies in channels. *J. Fluid Mech.* **252**, 647–666.

LIU, X., TANG, T., MOSTERT, W. & ADCOCK, T.A.A. 2025 Phase manipulation to analyse different types of nonlinearity using water waves as a case study. *Proc. R. Soc. A* **481** (2313), 20240831.

MALENICA, Š. & MOLIN, B. 1995 Third-harmonic wave diffraction by a vertical cylinder. *J. Fluid Mech.* **302**, 203–229.

MCIVER, M. & MCIVER, P. 2011 Water waves in the time domain. *J. Engng Maths* **70** (1), 111–128.

MEI, C.C. 1989 *The Applied Dynamics of Ocean Surface Waves*. World Scientific.

MEI, C.C. & LIU, L.F. 1973 The damping of surface gravity waves in a bounded liquid. *J. Fluid Mech.* **59** (2), 239–256.

MOLIN, B. & ETIENNE, S. 2000 On viscous forces on non-circular cylinders in low KC oscillatory flows. *Eur. J. Mech. B/Fluids* **19** (3), 453–457.

MOLIN, B., REMY, F., KIMMOUN, O. & STASSEN, Y. 2002 Experimental study of the wave propagation and decay in a channel through a rigid ice-sheet. *Appl. Ocean Res.* **24**, 247–260.

NEWMAN, J.N. 2017 *Marine Hydrodynamics*. MIT Press.

ORSZAGHOVA, J., TAYLOR, P.H., WOLGAMOT, H.A., MADSEN, F.J., PEGALAJAR-JURADO, A.M. & BREDMOSE, H. 2021 Wave- and drag-driven subharmonic responses of a floating wind turbine. *J. Fluid Mech.* **929**, A32.

PENALBA, M., GIORGI, G. & RINGWOOD, JV. 2017 Mathematical modelling of wave energy converters: a review of nonlinear approaches. *Renew. Sustain. Energy Rev.* **78**, 1188–1207.

SROKOSZ, M.A. 1980 Some relations for bodies in a canal, with an application to wave-power absorption. *J. Fluid Mech.* **99** (1), 145–162.

STOKES, G.G. 1851 On the effect of the internal friction of fluids on the motion of pendulums. *Trans. Camb. Phil. Soc.* **9**, 8–106.

TAN, B., ORSZAGHOVA, J., WOLGAMOT, H.A., KURNIAWAN, A. & TODALSHAUG, J.H. 2025 Third-order first-harmonic heave exciting forces on a small partially immersed sphere in long waves. *J. Fluid Mech.* **1009**, A62.

TAYLOR, P.H. & WILLIAMS, B.A. 2004 Wave statistics for intermediate depth water – NewWaves and symmetry. *J. Offshore Mech. Arctic Engng* **126** (1), 54–59.

TENG, B. & KATO, S. 2002 Third order wave force on axisymmetric bodies. *Ocean Engng* **29** (7), 815–843.

https://doi.org/10.1017/jfm.2026.11904 Published online by Cambridge University Press

TROMANS, P.S., ANATURK, A.R. & HAGEMEIJER, P. 1991 A new model for the kinematics of large ocean waves – application as a design wave. In *Proceedings of the First International Offshore and Polar Engineering Conference*, pp. 64–71. International Society of Offshore and Polar Engineers (ISOPE).

URSELL, F. 1952 Edge waves on a sloping beach. *Proc. R. Soc. Lond. A* **214** (1116), 79–97.

VAN DORN, W.G. 1966 Boundary dissipation of oscillatory waves. *J. Fluid Mech.* **24** (4), 769–779.

VANTORRE, M. 1986*a* On third-order radiation theory for axisymmetric bodies undergoing heave motion of multiple frequencies. *J. Engng Maths* **20** (3), 217–231.

VANTORRE, M. 1986*b* Third-order theory for determining the hydrodynamic forces on axisymmetric floating or submerged bodies in oscillatory heaving motion. *Ocean Engng* **13** (4), 339–371.

VANTORRE, M. 1990 Influence of draft variation on heave added-mass and hydrodynamic damping coefficients of floating bodies. *J. Ship Res.* **34** (3), 172–178.

VYZIKAS, T., STAGONAS, D., BULDAKOV, E. & GREAVES, D. 2018 The evolution of free and bound waves during dispersive focusing in a numerical and physical flume. *Coast. Engng* **132**, 95–109.

WALKER, D.A.G., TAYLOR, P.H. & EATOCK TAYLOR, R. 2004 The shape of large surface waves on the open sea and the Draupner New Year wave. *Appl. Ocean Res.* **26** (3–4), 73–83.

ZHAO, W., WOLGAMOT, H.A., TAYLOR, P.H. & EATOCK TAYLOR, R. 2017 Gap resonance and higher harmonics driven by focused transient wave groups. *J. Fluid Mech.* **812**, 905–939.

https://doi.org/10.1017/jfm.2026.11904 Published online by Cambridge University Press